



Quantitative contrast-enhanced optical coherence tomography

Yonatan Winetraub, Elliott D. SoRelle, Orly Liba, and Adam de la Zerda

Citation: [Applied Physics Letters](#) **108**, 023702 (2016); doi: [10.1063/1.4939547](https://doi.org/10.1063/1.4939547)

View online: <http://dx.doi.org/10.1063/1.4939547>

View Table of Contents: <http://scitation.aip.org/content/aip/journal/apl/108/2?ver=pdfcov>

Published by the [AIP Publishing](#)

Articles you may be interested in

[Ultra-high sensitive and high resolution optical coherence tomography using a laser induced electromagnetic dipole](#)

[Appl. Phys. Lett. **103**, 141118 \(2013\); 10.1063/1.4824493](#)

[Estimation of elasticity map of soft biological tissue mimicking phantom using laser speckle contrast analysis](#)
[J. Appl. Phys. **109**, 104704 \(2011\); 10.1063/1.3592352](#)

[Optical coherence tomography picorheology of biopolymer solutions](#)

[Appl. Phys. Lett. **92**, 173903 \(2008\); 10.1063/1.2917578](#)

[High-speed Signal Evaluation in Optical Coherence Tomography Based on Sub-Nyquist Sampling and Kalman Filtering Method](#)

[AIP Conf. Proc. **860**, 146 \(2006\); 10.1063/1.2361215](#)

[Multibeam interferometric illumination as the primary source of resolution in optical microscopy](#)

[Appl. Phys. Lett. **88**, 171112 \(2006\); 10.1063/1.2192153](#)



Quantitative contrast-enhanced optical coherence tomography

Yonatan Winetraub,^{1,2,3,4,a)} Elliott D. SoRelle,^{1,2,3,4,a)} Orly Liba,^{1,2,4,5}
and Adam de la Zerda^{1,2,3,4,5}

¹Molecular Imaging Program at Stanford, Stanford University, 299 Campus Drive, Stanford, California 94305, USA

²Bio-X Program, Stanford University, 299 Campus Drive, Stanford, California 94305, USA

³Biophysics Program, Stanford University, 299 Campus Drive, Stanford, California 94305, USA

⁴Department of Structural Biology, Stanford University, 299 Campus Drive, Stanford, California 94305, USA

⁵Department of Electrical Engineering, Stanford University, 299 Campus Drive, Stanford, California 94305, USA

(Received 10 August 2015; accepted 22 December 2015; published online 12 January 2016)

We have developed a model to accurately quantify the signals produced by exogenous scattering agents used for contrast-enhanced Optical Coherence Tomography (OCT). This model predicts distinct concentration-dependent signal trends that arise from the underlying physics of OCT detection. Accordingly, we show that real scattering particles can be described as simplified ideal scatterers with modified scattering intensity and concentration. The relation between OCT signal and particle concentration is approximately linear at concentrations lower than 0.8 particle per imaging voxel. However, at higher concentrations, interference effects cause signal to increase with a square root dependence on the number of particles within a voxel. Finally, high particle concentrations cause enough light attenuation to saturate the detected signal. Predictions were validated by comparison with measured OCT signals from gold nanorods (GNRs) prepared in water at concentrations ranging over five orders of magnitude (50 fM to 5 nM). In addition, we validated that our model accurately predicts the signal responses of GNRs in highly heterogeneous scattering environments including whole blood and living animals. By enabling particle quantification, this work provides a valuable tool for current and future contrast-enhanced *in vivo* OCT studies. More generally, the model described herein may inform the interpretation of detected signals in modalities that rely on coherence-based detection or are susceptible to interference effects. © 2016 AIP Publishing LLC.

[<http://dx.doi.org/10.1063/1.4939547>]

Optical Coherence Tomography (OCT) uses low coherence interferometry to obtain micron-resolution images of scattering samples.¹ While OCT has long been used for structural studies, it has only recently been explored for contrast-enhanced molecular imaging.^{2–4} However, for such contrast-enhanced OCT studies to reach their full potential, quantitative imaging capabilities during *in vivo* experiments are needed in order to assess biomarker expression levels,⁵ disease response to therapy,⁶ and developmental processes.⁷ Thus, the ability to easily extract quantitative information about scattering contrast agents will be useful for realizing OCT as a molecular modality. However, accurate quantitative measurements are not readily obtained from OCT images since detected signals comprise convoluted information from single and multiple scattering events as well as interference among photons within a given imaging volume.^{8,9} These effects impede quantification, especially in non-uniform scattering media such as biological tissues.¹⁰

Studies have previously modeled scattering in tissue phantoms using the independent scattering approximation, which yields signal linearity with concentration.¹¹ However, these models are only valid for low scatterer concentrations.^{12,13} Other work has assumed signal with a polynomial dependence on scatterer concentration.¹⁴ More recently, Mie theory and the extended Huygens-Fresnel (EHF) model have

been used to model scattering.^{15–18} These models have enabled quantification of tissue optical properties and highlight the non-linearity of OCT signal with increasing scatterer concentration. However, these models require the adjustment of many parameters and are limited in fundamental physical scope by the assumptions of Mie scattering. In addition, models of the signal properties of OCT contrast agents, particularly in biological tissues, have not yet been established.

Here, we report the development of a physical model to predict the OCT signal detected from nanoscale scattering particles. Unlike Mie and EHF models, our model assumes ray scattering principles and requires no *a priori* knowledge of particle-specific parameters or dominating physical scattering mechanisms. Therefore, the model is generally applicable to particles of any morphology and heterogeneous scattering environments. Using this approach, we accurately predicted concentration-dependent trends in the OCT signal from gold nanorods (GNRs) prepared in water, whole blood and injected intravenously into living mice.

We start with the highly simplified assumptions that (1) all particles within a sample reflect the same amount of light, A (i.e., the backscattering coefficient), (2) reflections are modeled by ray optics, and (3) multiply scattered photons within a single voxel are negligible (see supplementary material).²⁵ Under these assumptions, the electric field observed in a given imaging voxel represents the sum of the reflections

^{a)}Y. Winetraub and E. D. SoRelle contributed equally to this work.

from N particles within the voxel, depicted in Figure 1(a). These reflections can be treated as vectors of equal magnitude and random angle (phase). The angle θ_i between two vectors represents their difference in phase, and the OCT scattering intensity, X , detected from the two vectors can be analytically solved as a partial elliptical integral evaluated for all relative phase differences

$$X(2) = A/2\pi \int_0^{2\pi} \sqrt{(1 + \cos \theta)^2 + (\sin \theta)^2} d\theta. \quad (1)$$

Similarly, the mean vector for N scatterers can be computed by integrating $N - 1$ partial elliptical integrals that describe all inter-vector angles, which represent interference among the scatterers (often described as the sum of random phase vectors problem)

$$X(N) = A/(2\pi)^{N-1} \times \int_0^{2\pi} \int_0^{2\pi} \cdots \int_0^{2\pi} \sqrt{\left(1 + \sum_i \cos \theta_i\right)^2 + \left(\sum_i \sin \theta_i\right)^2} \times d\theta_1 \dots d\theta_{N-1}. \quad (2)$$

We used a Monte Carlo simulation to estimate the integral result (Eq. (S5), Figure S1), which led to the following model for the mean scattering electric field magnitude. In Spectral Domain OCT (SD-OCT), the cross-correlation term is used to assess the signal from the sample. This term (speckle intensity) is linear with the electric field.¹⁹ The mean magnitude of speckle intensity, X , in a voxel as a function of N is

$$X(N) = \begin{cases} A & N = 1 \\ 0.89A\sqrt{N} & N \geq 2, \end{cases} \quad (3)$$

where A is the OCT intensity of a single particle. Interestingly, summing the random phase vectors is analogous to a 2D random walk²⁰ in which the length of the resulting mean vector is proportional to \sqrt{N} and A (Figure 1(b)). As a note, the speckle pattern becomes more fully developed as N increases. However, we use the mean speckle intensity and thus do not require full Rayleigh distribution terms.

The number of scatterers, N , in a voxel follows a Poisson distribution with a mean of λ , where λ is the expected number of particles per voxel. Thus, the expected OCT intensity is

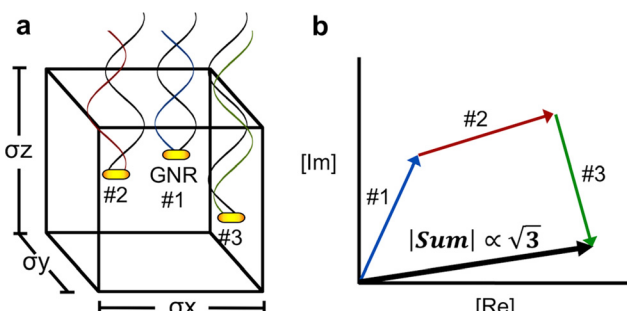


FIG. 1. (a) Schematic of interference of GNRs in an imaging voxel. For illustration purposes, we depict the voxel as a cube. In reality, the voxel is optically determined and thus ellipsoid in shape. (b) A vector sum of the scattered photons, each with random phase.

$$\bar{I} = \bar{I}(N = 1) \times P(N = 1) + \sum_{k=2}^{\infty} \bar{I}(N = k) \times P(N = k), \quad (4a)$$

where the probability of having $N = k$ particles in a voxel is described by the Poisson distribution

$$P(N = k) = \lambda^k / k! \times e^{-\lambda}. \quad (4b)$$

Substituting (3) and (4b) into (4a) provides a full description of the mean OCT intensity observed from N scatterers per voxel

$$\bar{I} = A \times \lambda \times e^{-\lambda} + 0.89 \times A \times \sum_{k=2}^{\infty} \sqrt{k} \times \lambda^k / k! \times e^{-\lambda}. \quad (5a)$$

Eq. (5a) describes the expected speckle intensity from an ideal scatterer. However, real contrast agents such as GNRs are not ideal; these particles reflect varying amounts of light depending on their relative angular orientation to the incident beam, distance from the beam center, and other physical considerations. Despite these factors, we mathematically proved that any scatterer with a speckle intensity distribution function $P(A)$ can be described as an ideal scatterer with an effective speckle intensity C_1 and effective number of particles per voxel C_2 , which are respectively defined as $C_1 = E[A^2]/E[A]$ and $C_2 = E[A^2]/E^2[A]$ (for the full proof, see supplementary material).²⁵ Using these definitions, Eq. (5a) can be rewritten as

$$\bar{I} = C_1 \times (\lambda/C_2) \times e^{-(\lambda/C_2)} + 0.89 \times C_1 \times \sum_{k=2}^{\infty} \sqrt{k} \times (\lambda/C_2)^k / k! \times e^{-(\lambda/C_2)}. \quad (5b)$$

Eq. (5b) generates a full model for scattering when multiplied by an exponential decay to account for light attenuation, as predicted by the Beer-Lambert Law (Eqs. (S17)–(S18)). Consequently, this model can describe nearly any sample that reflects light by adjusting the effective concentration and brightness (see supplementary material for further description and examples).²⁵ For low particle concentrations, $\lambda \ll 1$ and $P(N \geq 2) \ll P(N = 1)$. In this case, the average speckle intensity is simply the average number of particles per voxel times the per particle intensity. When $\lambda \gg 1$, the Poisson distribution is a Gaussian distribution and the average speckle intensity is approximated as follows (see supplementary material for derivation):²⁵

$$\bar{I}(\lambda) \approx \begin{cases} C_1/C_2 \times \lambda & \lambda \ll 1 \\ 0.89 \times C_1 \times \sqrt{(\lambda/C_2)} & \lambda \gg 1. \end{cases} \quad (6)$$

Eq. (6) predicts two distinct regimes of signal increase with increasing particle concentration. Speckle intensity increases linearly with low concentrations. At higher concentrations, the speckle intensity increases as the square root of the number of scatterers due to inter-voxel interference. We calculated the transition between these phases, $\lambda_{crit} = 0.8 \times C_2$ (Eq. (S15)).

We tested our model against measured OCT signals from varying concentrations of GNRs in distilled deionized (DDI) water. GNRs ($100\text{ nm} \times 30\text{ nm}$, peak resonance = 800 nm, Figure S13) were synthesized using a method adapted from Ye *et al.*²¹ and stabilized with poly(sodium-4-styrenesulfonate) (PSS, MW 70 kDa) as previously reported.²² GNRs were prepared at concentrations ranging from 50 fM (2×10^7 NPs/ml) to 5 nM (2×10^{12} NPs/ml) and then imaged in square-shaped glass capillary tubes (Figure 2(a)) using a commercial spectral domain OCT system (Ganymede HR SD-OCT, ThorLabs, Newton, NJ). The SD-OCT light source was a superluminescent diode (SLD) with a center wavelength of 900 nm and a spectral bandwidth of 200 nm. The voxel size determined by the optical beam waist (x, y) and coherence length (z) was $8\text{ }\mu\text{m} \times 8\text{ }\mu\text{m} \times 2\text{ }\mu\text{m}$ (Full Width Half Max), and the SNR (Signal to Noise Ratio) was 106 dB. Figure 2(b) shows that below $\lambda_{crit} = 40\text{ pM}$ (which corresponded to ~ 0.8 effective GNR per voxel), the increase in GNR OCT signal (red points) with concentration is roughly linear (black curve). However, the OCT signal measured from higher GNR concentrations increases by following a \sqrt{N} dependence (magenta curve). At sufficiently high concentrations, the observed OCT signal deviates even further from the \sqrt{N} prediction. This deviation occurs at the shadowing limit (dashed green vertical line)—the concentration of GNRs at which highest detectable signal is achieved near the top of the sample and deeper regions exhibits

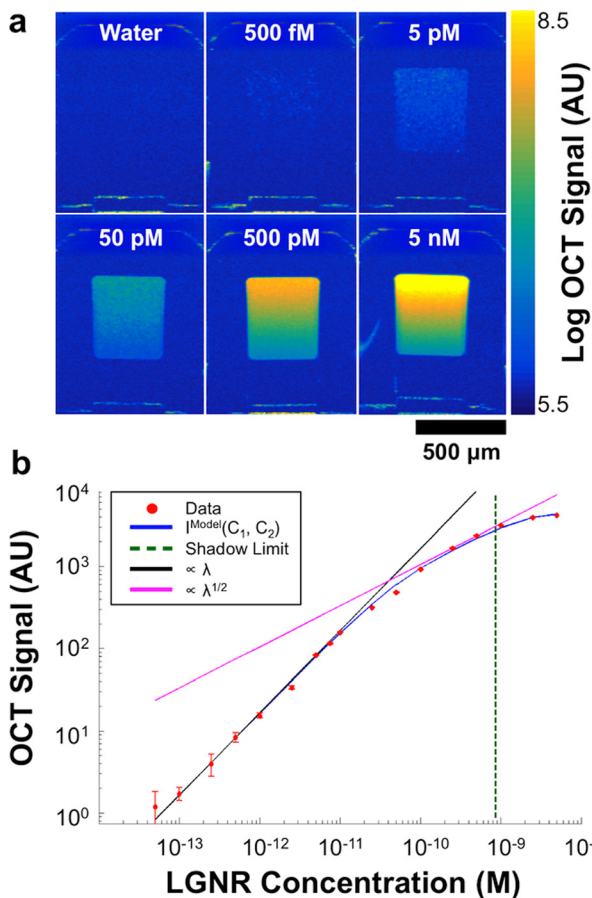


FIG. 2. (a) Mean measured ROI (Region of Interest) OCT signal from various GNR concentrations. (b) Model (blue) and experimental data (red) ($R^2 = 0.998$). Linear (black) and square root (magenta) fits are also shown, along with the predicted shadowing limit (dashed green). Data are presented as mean \pm S.E.M ($n = 3$ for each concentration).

reduced or no signal due to photon attenuation. While linear square root models fit the data in certain concentration regimes, our model (depicted in blue) displays a highly correlated fit across all concentrations ($R^2 = 0.998$). This model was calculated using Eq. (5b), where C_1 , C_2 , and ϵ (the extinction coefficient) were fit to the data using a least squares approximation. The best fit occurred for $C_2 = 3.9$.

We further confirmed this result by showing that values of $E[A]$ and $E[A^2]$ experimentally measured from low GNR concentrations were consistent with the C_1 and C_2 values obtained by fitting a large range of concentrations. This means that scattering intensity for high concentrations can be explained using data from low concentration tubes only (see supplementary material).²⁵

We next tested our model's ability to fit GNR signal in the presence of biological scattering environments. GNRs were prepared at various concentrations in freshly excised mouse blood. The final concentration of blood components in each sample was 90% of the original concentration in whole blood (for example, 10 μl of GNR solution and 90 μl of whole blood were mixed to produce the desired GNR concentration in 90% blood). OCT images were acquired as before (Figure 3(a)). We were able to distinguish GNRs from blood at concentrations as low as 5 pM ($p < 0.01$), which corresponds to less than one effective GNR per voxel on average. We predicted (as described in the supplementary material) that the square root regime for GNRs in blood would exhibit the same C_1 and C_2 as GNRs in water.²⁵ As shown in Figure 3(b), this prediction (blue line) accurately describes the experimental data (red points, $R^2 = 0.971$). Interestingly, none of the measured signals from GNRs in blood fell within the linear regime. We attribute this to the strong interaction of light with blood, which creates multiple scattering trajectories (see supplementary material).²⁵

As a final demonstration, we fit the signals from known GNR concentrations acquired during intravenous injections into living nude (nu^-/nu^-) mice ($n = 3$). Each mouse was anesthetized with 2% isoflurane, and a total of 250 μl of 23.5 nM GNRs were tail-vein injected sequentially in 20 μl increments. After each incremental injection, GNRs were allowed to circulate for 1 min and an image of the right ear pinna (shown in Figure 4(a)) was acquired. This process allowed us to measure the concentration-dependent OCT signal of GNRs *in vivo*. Figures 4(b)–4(c) show representative OCT images before and after incremental injections. As with *in vitro* experiments, we predicted that the same parameters and square root regime would provide a good prediction for *in vivo* data. Unlike the *in vitro* experiments, lighting conditions L (i.e., attenuation by tissue above the analyzed blood vessels) are unknown. Furthermore, light shadowing from high GNR concentration must also be considered by accounting for the vessel diameter D

$$\bar{I}(\lambda) = [0.89 \times L \times C_1 \times \sqrt{\lambda/C_2} \times (1 - 10^{-2 \times c \times \epsilon \times D})] / [2 \times c \times \epsilon \times D \times \log 10], \quad (7)$$

where C_1 , C_2 , and ϵ are taken from the fit for GNRs in water. λ and c are GNR concentrations per voxel and in molarity, respectively. Both D and L should be fitted for each

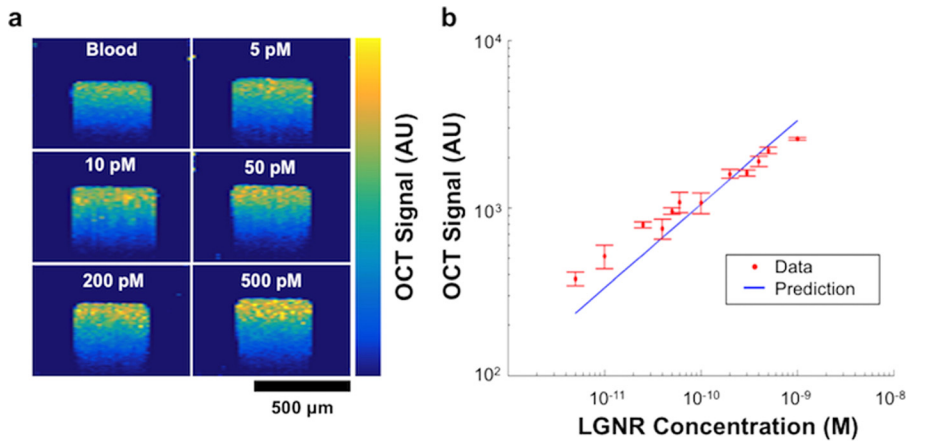


FIG. 3. (a) OCT intensity signal from GNRs in whole mouse blood. (b) Model prediction (blue) and measured signals of GNRs in blood ($R^2 = 0.971$).

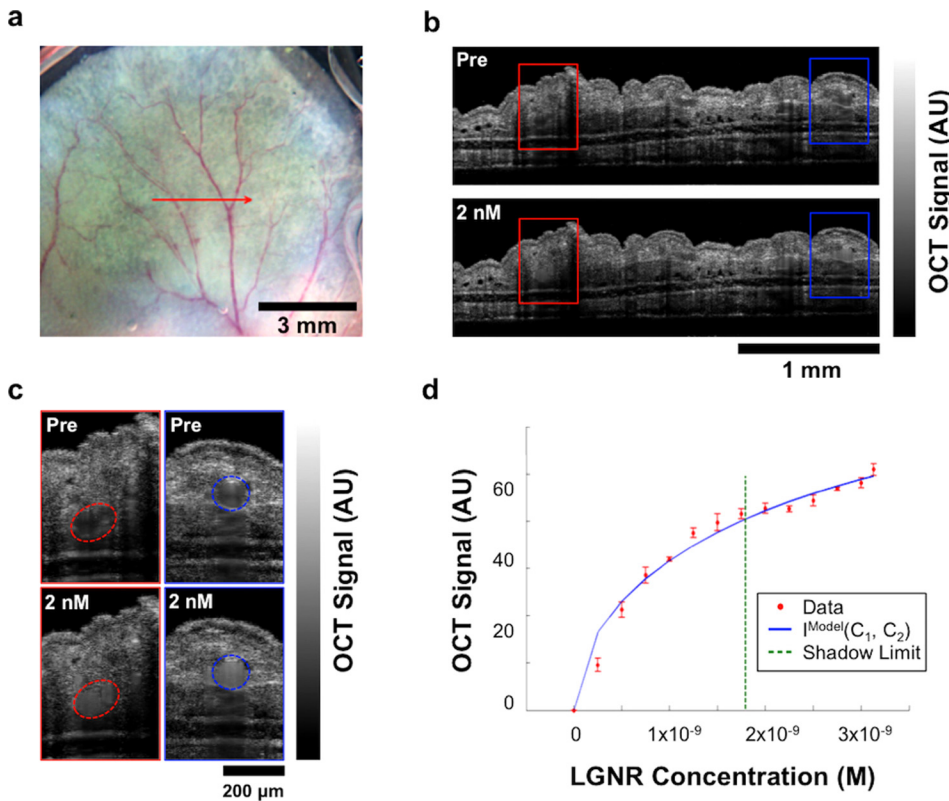


FIG. 4. (a) Photograph of a mouse ear pinna and vasculature imaged with OCT. The horizontal red line denotes the location of the acquired B-scan. (b) OCT intensity images of healthy mouse ear vasculature before and after incremental intravenous injection of GNRs. (c) Zoomed images of representative blood vessels marked by red and blue rectangles in (b). Vessels exhibit greater OCT intensity as the concentration of GNRs in circulation increases. (d) Quantification of OCT intensity increases due to GNR concentration in blood vessels of healthy mice ($n=9$; 3 vessels for each of 3 mice).

individual blood vessel (see Figure S18 for individual vessel plots). Eq. (7) fits the *in vivo* data well ($R^2 = 0.978$), as shown in Figure 4(d).

In summary, we describe a simple model for quantifying contrast-enhanced OCT signal based on the number of scattering agents within the imaging volume. Importantly, real particles can be described as ideal scatterers with modified speckle intensity and concentration. This model accurately describes experimental results for GNR contrast agents in water, blood, and *in vivo*. This model enables the extraction of quantitative measurements from OCT images provided only that expected speckle intensity can be estimated by averaging samples spatially or over time.

Because of its simplicity and generality, we expect that this model can be readily adapted to enable quantitative capabilities for contrast-enhanced OCT studies. This ability will aid the ongoing development of OCT as a molecular

imaging modality. The principles of this model may also be adapted to enable quantitative analysis in other imaging methods that suffer from multiple scattering and interference effects, most notably ultrasound and contrast-enhanced ultrasound.^{23,24}

We would like to acknowledge the funding from the following sources: the United States Air Force (FA9550-15-1-0007), the National Institutes of Health (NIH DP50D012179), the National Science Foundation (NSF 1438340), the Damon Runyon Cancer Research Center (DFS# 06-13), the Susan G. Komen Breast Cancer Foundation (SAB15-00003), the Mary Kay Foundation (017-14), the Donald E. and Delia B. Baxter Foundation, a seed grant from the Center for Cancer Nanotechnology Excellence and Translation (CCNE-T U54CA151459), and a Stanford Bio-X Interdisciplinary Initiative Seed Grant for

GNR characterization. Additional thanks to the Cell Sciences Imaging Facility (CSIF), the Stanford Nano Center (SNF), and the Stanford Nanocharacterization Lab (SNL) for access to instruments for GNR characterization. Special thanks to Dr. Matthew Lew for insightful discussions.

- ¹D. Huang, E. A. Swanson, C. P. Lin, J. S. Schuman, W. G. Stinson, W. Chang, M. R. Hee, T. Flotire, K. Gregory, C. A. Puliafito, and J. G. Fujimoto, *Science* **254**, 1178 (1991).
- ²T. M. Lee, A. L. Oldenburg, S. Sifatfalwalla, D. L. Marks, W. Luo, F. J.-J. Toublan, K. S. Suslick, and S. A. Boppart, *Opt. Lett.* **28**, 1546 (2003).
- ³A. L. Oldenburg, M. N. Hansen, D. A. Zweifel, A. Wei, and S. A. Boppart, *Opt. Express* **14**, 6724 (2006).
- ⁴T. S. Troutman, J. K. Barton, and M. Romanowski, *Opt. Lett.* **32**, 1438 (2007).
- ⁵X. Chen, P. S. Conti, and R. A. Moats, *Cancer Res.* **64**, 8009 (2004).
- ⁶F. G. Blankenberg, P. D. Katsikis, J. F. Tait, R. E. Davis, L. Naumovski, K. Ohtsuki, S. Kopiwoda, M. J. Abrams, M. Darkes, R. C. Robbins, H. T. Maecker, and H. W. Strauss, *Proc. Natl. Acad. Sci. U.S.A.* **95**, 6349 (1998).
- ⁷R. Tomer, K. Khairy, F. Amat, and P. J. Keller, *Nat. Methods* **9**, 755 (2012).
- ⁸A. F. Fercher, *J. Biomed. Opt.* **1**, 157 (1996).
- ⁹J. M. Schmitt, S. H. Xiang, and K. M. Yung, *J. Biomed. Opt.* **4**, 95 (1999).
- ¹⁰J. M. Schmitt, A. Knuttel, M. Yadlowsky, and M. A. Eckhaus, *Phys. Med. Biol.* **39**, 1705 (1994).
- ¹¹D. J. Faber and T. G. van Leeuwen, *Opt. Lett.* **34**, 1435 (2009).
- ¹²L. L. Foldy, *Phys. Rev.* **67**, 107 (1945).
- ¹³M. Lax, *Rev. Mod. Phys.* **23**, 287 (1951).
- ¹⁴G. Zaccanti, S. Del Bianco, and F. Martelli, *Appl. Opt.* **42**, 4023 (2003).
- ¹⁵J. Kalkman, A. V. Bykov, D. J. Faber, and T. G. van Leeuwen, *Opt. Express* **18**, 3883 (2010).
- ¹⁶V. D. Nguyen, D. J. Faber, E. van der Pol, T. G. van Leeuwen, and J. Kalkman, *Opt. Express* **21**, 29145 (2013).
- ¹⁷J. C. Y. Kah, T. H. Chow, B. K. Ng, S. G. Razul, M. Olivo, and C. J. R. Sheppard, *Appl. Opt.* **48**, D96 (2009).
- ¹⁸P. E. Andersen, T. M. Jorgensen, L. Thrane, A. Tycho, and H. T. Yura, *Optical Coherence Tomography*, edited by W. Drexler and J. G. Fujimoto (Springer, 2015), Chap. 3.
- ¹⁹A. Fercher, W. Drexler, C. K. Hitzenberger, and T. Lasser, *Rep. Prog. Phys.* **66**, 239 (2003).
- ²⁰J. Goodman, *Speckle Phenomena in Optics: Theory and Applications*, 1st ed. (Roberts & Co., Greenwood Village, CO, 2008).
- ²¹X. Ye, C. Zheng, J. Chen, Y. Gao, and C. B. Murray, *Nano Lett.* **13**, 765 (2013).
- ²²E. D. SoRelle, O. Liba, Z. Hussain, M. Gambhir, and A. de la Zerda, *Langmuir* **31**, 12339 (2015).
- ²³K. Z. Abd-Elmoniem, A.-B. M. Youssef, and Y. M. Kadah, *IEEE Trans. Biomed. Eng.* **49**, 997 (2002).
- ²⁴F. Kiessling, S. Fokong, P. Koczera, W. Lederle, and T. Lammers, *J. Nucl. Med.* **53**, 345 (2012).
- ²⁵See supplementary material at <http://dx.doi.org/10.1063/1.4939547> for model derivations and proofs as well as information regarding imaging experiments and gold nanorods used in this study.